



nature nanotechnology

JULY 2011 VOL 6 NO 7
www.nature.com/naturenanotechnology

SUPERCONDUCTIVITY
Electrostatic doping pays off

SURFACE SCIENCE
Ultracold microscopy

NANOPARTICLES
Feel the heat

Printing flexible nanomaterials

Report Documentation Page				Form Approved OMB No. 0704-0188	
Public reporting burden for the collection of information is estimated to average 1 hour per response, including the time for reviewing instructions, searching existing data sources, gathering and maintaining the data needed, and completing and reviewing the collection of information. Send comments regarding this burden estimate or any other aspect of this collection of information, including suggestions for reducing this burden, to Washington Headquarters Services, Directorate for Information Operations and Reports, 1215 Jefferson Davis Highway, Suite 1204, Arlington VA 22202-4302. Respondents should be aware that notwithstanding any other provision of law, no person shall be subject to a penalty for failing to comply with a collection of information if it does not display a currently valid OMB control number.					
1. REPORT DATE JUL 2011		2. REPORT TYPE		3. DATES COVERED 00-00-2011 to 00-00-2011	
4. TITLE AND SUBTITLE Large-Area Flexible 3D Optical Negative Index Metamaterial Formed By Nanotransfer Printing				5a. CONTRACT NUMBER	
				5b. GRANT NUMBER	
				5c. PROGRAM ELEMENT NUMBER	
6. AUTHOR(S)				5d. PROJECT NUMBER	
				5e. TASK NUMBER	
				5f. WORK UNIT NUMBER	
7. PERFORMING ORGANIZATION NAME(S) AND ADDRESS(ES) US Navy NAVAIR-NAWCWD, Research and Intelligence Department, Chemistry Branch, China Lake, CA, 93555				8. PERFORMING ORGANIZATION REPORT NUMBER	
9. SPONSORING/MONITORING AGENCY NAME(S) AND ADDRESS(ES)				10. SPONSOR/MONITOR'S ACRONYM(S)	
				11. SPONSOR/MONITOR'S REPORT NUMBER(S)	
12. DISTRIBUTION/AVAILABILITY STATEMENT Approved for public release; distribution unlimited					
13. SUPPLEMENTARY NOTES Nature Nanotechnology, Volume: 6, Pages: 402-407, July 2011					
14. ABSTRACT Negative-index metamaterials (NIMs) are engineered structures with optical properties that cannot be obtained in naturally occurring materials^{1,3}. Recent work has demonstrated that focused ion beam⁴ and layer-by-layer electron-beam lithography⁵ can be used to pattern the necessary nanoscale features over small areas (hundreds of mm²) for metamaterials with three-dimensional layouts and interesting characteristics including negative-index behaviour in the optical regime. A key challenge is in the fabrication of such three-dimensional NIMs with sizes and at throughputs necessary for many realistic applications (including lenses, resonators and other photonic components^{6,8}). We report a simple printing approach capable of forming large-area, high-quality NIMs with three-dimensional, multilayer formats. Here, a silicon wafer with deep, nanoscale patterns of surface relief serves as a reusable stamp. Blanket deposition of alternating layers of silver and magnesium fluoride onto such a stamp represents a process for 'inking' it with thick, multilayer assemblies. Transfer printing this ink material onto rigid or flexible substrates completes the fabrication in a high-throughput manner. Experimental measurements and simulation results show that macroscale, three-dimensional NIMs (>75 cm²) nano-manufactured in this way exhibit a strong, negative index of refraction in the near-infrared spectral range, with excellent figures of merit.					
15. SUBJECT TERMS					
16. SECURITY CLASSIFICATION OF:			17. LIMITATION OF ABSTRACT Same as Report (SAR)	18. NUMBER OF PAGES 15	19a. NAME OF RESPONSIBLE PERSON
a. REPORT unclassified	b. ABSTRACT unclassified	c. THIS PAGE unclassified			

Large-area flexible 3D optical negative index metamaterial formed by nanotransfer printing

Debashis Chanda¹, Kazuki Shigeta¹, Sidhartha Gupta¹, Tyler Cain¹, Andrew Carlson¹, Agustin Mihai¹, Alfred J. Baca³, Gregory R. Bogart⁴, Paul Braun¹ and John A. Rogers^{1,2*}

Negative-index metamaterials (NIMs) are engineered structures with optical properties that cannot be obtained in naturally occurring materials^{1–3}. Recent work has demonstrated that focused ion beam⁴ and layer-by-layer electron-beam lithography⁵ can be used to pattern the necessary nanoscale features over small areas (hundreds of μm^2) for metamaterials with three-dimensional layouts and interesting characteristics, including negative-index behaviour in the optical regime. A key challenge is in the fabrication of such three-dimensional NIMs with sizes and at throughputs necessary for many realistic applications (including lenses, resonators and other photonic components^{6–8}). We report a simple printing approach capable of forming large-area, high-quality NIMs with three-dimensional, multilayer formats. Here, a silicon wafer with deep, nanoscale patterns of surface relief serves as a reusable stamp. Blanket deposition of alternating layers of silver and magnesium fluoride onto such a stamp represents a process for ‘inking’ it with thick, multilayer assemblies. Transfer printing this ink material onto rigid or flexible substrates completes the fabrication in a high-throughput manner. Experimental measurements and simulation results show that macroscale, three-dimensional NIMs ($>75\text{ cm}^2$) nano-manufactured in this way exhibit a strong, negative index of refraction in the near-infrared spectral range, with excellent figures of merit.

NIMs have values of permittivity and permeability that are simultaneously negative over certain ranges of frequencies^{1–3}. Building on original work with structures designed to operate in the microwave regime, recent efforts have demonstrated NIMs for terahertz^{9,10} and even optical^{11–13} frequencies. Trilayer stacks of metal–dielectric–metal with total thicknesses of $\sim 100\text{ nm}$, patterned using conventional planar techniques into two-dimensional (2D) mesh (fishnet) layouts with characteristic sizes in the range of $100\text{--}500\text{ nm}$ yield some of the best examples of optical NIMs for the NIR wavelength range^{11,14,15}. Recent theoretical^{14,16} and experimental work⁴ suggests that stacking up many layers of such 2D NIMs produces cascading effects and a strong mutual inductance coupling between neighbouring layers (LC resonators). The result is a three-dimensional (3D) NIM with a broadband negative index of refraction and relatively low loss^{17,18}. The only reported structure of this type was fabricated in serial processes using focused ion beam (FIB) lithography⁴ to machine arrays of holes in a uniform metal/dielectric multilayer coating. Although this method provides the necessary submicrometre resolution and excellent control over out-of-plane geometries, its practical use is restricted to overall lateral dimensions of less than $20\text{ }\mu\text{m}$ (ref. 4). This size limitation, taken together with the complexity of the lithography tools and

their extremely slow patterning speeds, make this technique poorly suited to requirements for realistic applications including superlenses and photonic components, where cost, throughput, area coverage and long-range uniformity are important considerations. Alternative approaches to 3D nanofabrication, such as those based on colloidal self-assembly, interference lithography and two-photon polymerization-based direct laser writing lack the ability to embed multiple metal/dielectric layers over a 3D space. Nanoimprint lithography^{19,20} and various forms of soft lithography^{21–25}, in their standard embodiments, offer the necessary resolution, but they do not form 3D structures easily. In the following, we describe a 3D transfer printing method that is directly applicable to the fabrication of 3D NIMs with excellent optical characteristics, in ways that are scalable to arbitrarily large areas and that are compatible with manufacturing. We use the resulting methods to fabricate 3D NIMs with 11 layers and submicrometre unit cell dimensions, over areas of $>75\text{ cm}^2$, corresponding to $>10^5 \times 10^5$ unit cells, all with excellent uniformity and minimal defects. The area and number of unit cells both correspond to increases of more than a factor of 2×10^7 over previous reports⁴. Multiple cycles of printing with a single stamp demonstrate use in a manufacturing mode at throughputs that are $\sim 1 \times 10^8$ times higher than those possible with state-of-the-art FIB systems ($\sim 2.5\text{ s}$ per unit cell). Optical measurements and calculations show negative index of refraction in the near-infrared (NIR) spectral range, with values as large as $\text{Re}(n) \approx -7$ at $\lambda = 2.4\text{ }\mu\text{m}$ and high figures of merit (FOM) of ~ 8 at $\lambda = 1.95\text{ }\mu\text{m}$, indicating the comparatively low-loss nature of these large-area printed 3D NIMs. The outcomes compare favourably with small-scale 3D NIMs formed by FIB, where $\text{Re}(n) \approx -1.5$ at $\lambda = 1.775\text{ }\mu\text{m}$ and $\text{FOM} \approx 3$ at $\lambda = 1.8\text{ }\mu\text{m}$ (ref. 4).

Figure 1 shows the three main steps used in the fabrication: (i) ‘inking’ a stamp with a solid, multilayer stack deposited by electron-beam evaporation with a collimated, normally incident flux of material, (ii) contacting this stamp against a target substrate to ‘print’ a patterned multilayer structure by transfer of material deposited on the raised regions, and (iii) removal of the unprinted material from the stamp to prepare it for another round of printing. For the cases described here, the stamps consist of silicon wafers, anisotropically etched in the required geometry through polymer masks defined by soft nanoimprint lithography. Many stamps can be produced with a single imprint mould, and each stamp can be used many times for printing. The depth of etching ($\sim 1\text{ }\mu\text{m}$) in the present case exceeds the total thickness of the deposited multilayer stack (430 nm), which consists of alternating layers of silver (30 nm) and MgF_2 (50 nm) on top of a sacrificial layer of SiO_2

¹Departments of Materials Science and Engineering, Beckman Institute, and Frederick Seitz Materials Research Laboratory, University of Illinois at Urbana-Champaign, Urbana, Illinois 61801, USA, ²Department of Mechanical Science and Engineering, University of Illinois at Urbana-Champaign, Urbana, Illinois 61801, USA, ³US Navy NAVAIR-NAWCWD, Research and Intelligence Department, Chemistry Branch, China Lake, California 93555, USA, ⁴Sandia National Laboratories, Albuquerque, New Mexico, USA. *e-mail: jrogers@uiuc.edu

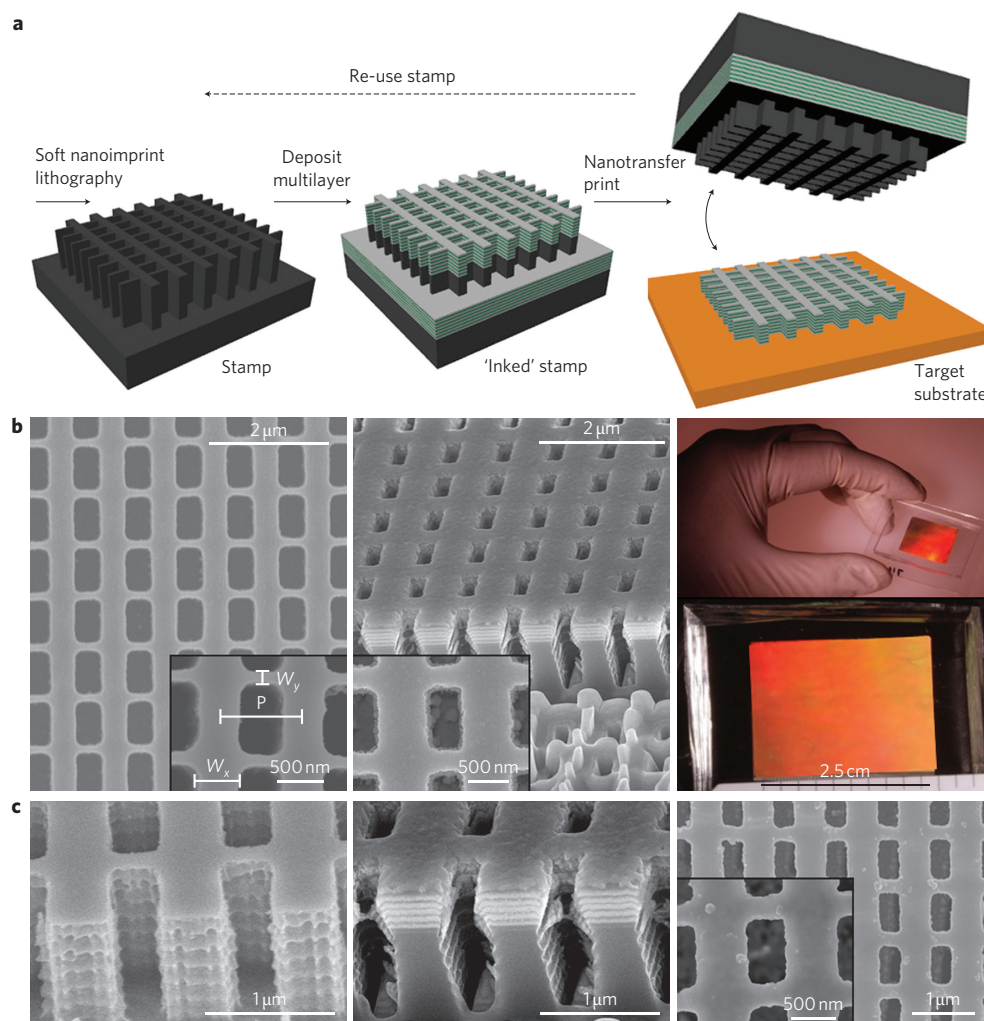


Figure 1 | Fabricating 3D NIMs by transfer printing. **a**, Schematic of steps for printing. **b**, Top-view SEM image of a silicon stamp (left; inset, magnified view), tilted view (52°) SEM image of a stack of alternating layers of Ag and MgF_2 on a silicon stamp (middle; inset, magnified top view), cross-sectioned by FIB, and a macroscopic optical image of a large ($\sim 2.5 \times 2.5$ cm) printed 3D NIM (right). **c**, Corresponding SEM images of a tilted silicon stamp (left), an eleven-layer Ag/ MgF_2 stack (middle) and a printed 3D NIM (right; inset, magnified top view). Period P of the structure is 850 nm, and the depth-averaged widths of the ribs in the fishnet along the x - and y -directions are 635 nm (W_x) and 225 nm (W_y), respectively. The thicknesses of the Ag and MgF_2 layers are 30 and 50 nm, respectively.

(50 nm) designed to facilitate release during the printing. The vertical dimension is defined by metal/dielectric stacks with individual thicknesses that are subwavelength in dimension. These materials offer effective media where the origin of negative-index behaviour emerges from capacitive and inductive coupling between the constituent layers^{14,17}. Plan- and tilted-view scanning electron microscope (SEM) images of a stamp before and after multilayer deposition appear in the left and middle frames of Fig. 1b,c, respectively. The inset in the left frame of Fig. 1b identifies the key geometrical parameters of the relief on the stamp. During electron-beam evaporation of the multilayer stack, deposits form not only on the flat raised and recessed regions of the stamps but also on protruding structures on the sidewalls that result from the Bosch ICP-RIE etching process. These deposits, which appear most prominently near the tops of the sidewalls (Fig. 1, Supplementary Fig. S3), are not transferred in the printing process. The slightly non-vertical sidewalls ($\sim 6\text{--}8^\circ$) in the multilayer structures on the raised regions of the stamps (middle frames, Fig. 1b,c) result from diffusion and grain growth during evaporation, primarily in the MgF_2 layers (Supplementary Fig. S3), consistent with known phenomena in physical vapour deposition^{26,27} rather than from

incomplete collimation of the evaporator systems. The sidewall angles are comparable to, or somewhat larger than, those achieved with FIB⁴. In the next step, contact printing delivers the multilayer deposits on the raised regions of the stamp to a target substrate, facilitated by removal of the SiO_2 release layer with dilute hydrofluoric acid, as described in the Methods and Supplementary Information. A printed structure (area, 6.5 cm^2) on a polydimethyl-siloxane (PDMS) substrate is shown in the right frames of Fig. 1b. This 3D NIM includes 11 layers (Ag on top of five repeats of MgF_2/Ag) in a fishnet geometry, where the period P is 850 nm, and the depth-averaged widths of the ribs along the x - and y -directions are 635 nm (W_x) and 225 nm (W_y), respectively (right frame, Fig. 1c), consistent with the geometry of the relief on the stamp (left frame, Fig. 1b) and the sidewall angle of the multilayer. Figure 2 provides a large-area SEM image (Fig. 2a) and magnified top (Fig. 2c) and cross-sectional (Fig. 2b) views of regions of a representative sample printed on PDMS. The printing process flips the structure, as is evident by comparing the cross-sectional view in Fig. 2b to those in the middle frames of Fig. 1b and c; no other changes are visible. This robust operation in printing is owing, in part, to the favourable mechanical properties of the multilayer

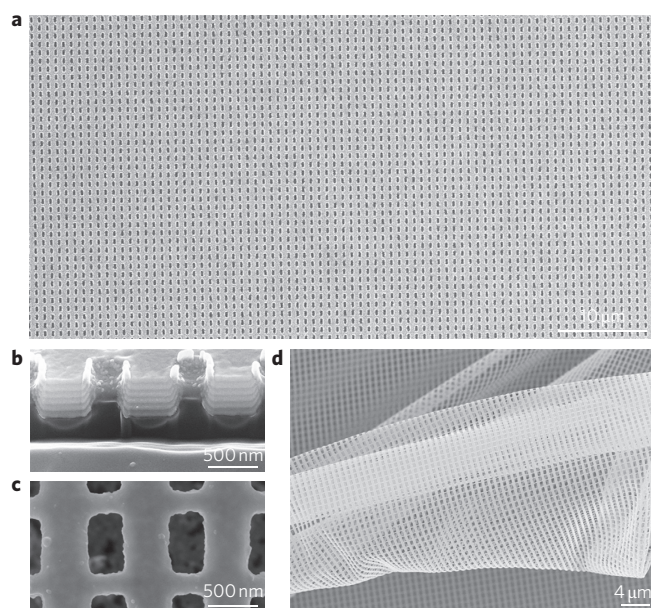


Figure 2 | Large-area, printed 3D NIMs in supported and free-standing configurations. **a**, Large-area SEM image of a representative region of a printed 3D NIM. **b, c**, SEM images of cross-sectional (FIB milled) and top views of this structure. **d**, SEM image of a flexible 3D NIM membrane formed by release and subsequent deposition on a solid support.

fishnet stacks, as revealed in the image shown in Fig. 2d of a quasi free-standing 3D NIMs membrane, created by release from a stamp and solution deposition onto a solid support. The absence of cracking or tearing suggests surprisingly high levels of physical toughness and mechanical flexibility. Although such structures are mechanically robust, handling or otherwise manually manipulating them is difficult owing to their exceptionally low bending stiffnesses. As a result, practical applications require a supporting substrate of some type. In addition to facilitating the printing process, this mechanics (Supplementary Fig. S4) might also enable wrapping of curved surfaces for integration with refractive lenses or other substrates of interest^{28–30}, or folding to increase the overall thickness of the material. Mechanical stacking of 3D NIMs like those shown here represents a conceivable strategy for achieving even larger thicknesses, although overlay registration requirements of ~50–60 nm create some engineering challenges. Although negative-index behaviour occurs only for normally incident light, mechanical flexibility can be useful to (i) facilitate installation of NIMs into systems that make use of planar geometries, (ii) enable mounting of NIMs on curved substrates in which operation only occurs on light that is incident in locally normal configurations and/or (iii) impart NIMs with a level of mechanical robustness that cannot be achieved in rigid, brittle formats. To demonstrate the large-area scalability of this process, we built macroscale 3D NIMs with dimensions of 8.7 cm × 8.7 cm, limited only by the sizes of the available stamps. Figure 3a shows a large silicon stamp ‘inked’ with an 11-layer stack. A representative 3D NIM printed from such a stamp onto a flexible PDMS substrate is shown in Fig. 3b. The fabrication process is

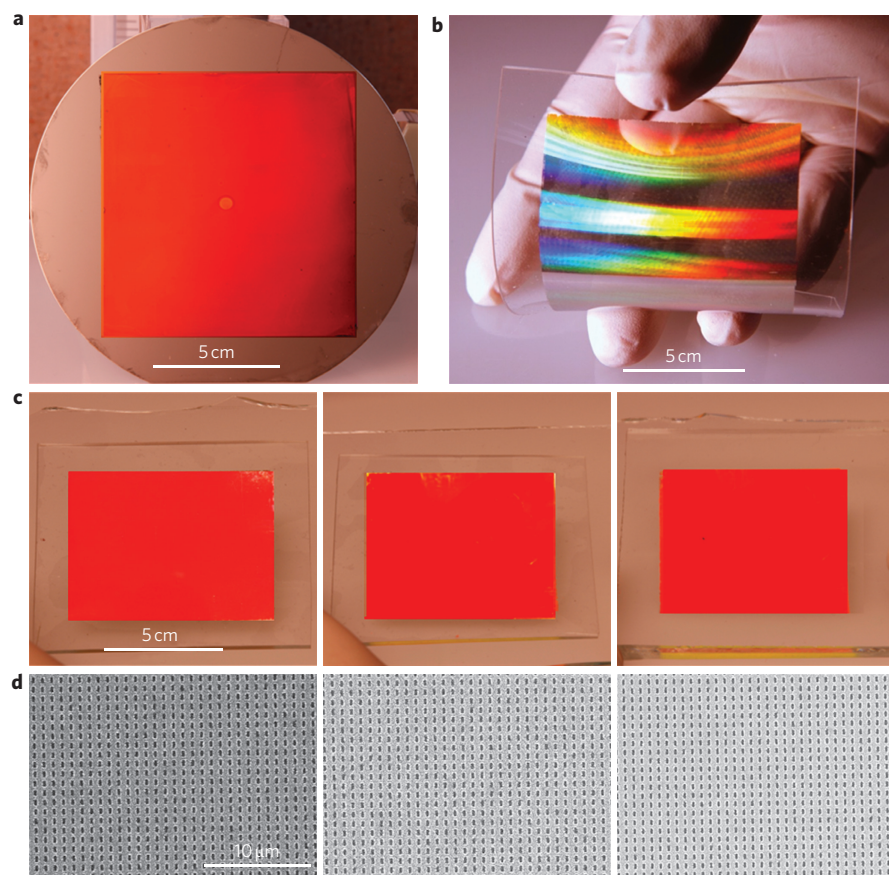


Figure 3 | Macroscale, printed 3D NIMs and demonstration of use in a repetitive ‘manufacturing’ mode. **a**, Macroscopic optical image of a 10 cm × 10 cm multilayer deposit on a large-area silicon stamp. **b**, 3D NIM printed with such a stamp onto a flexible substrate, in a single step. **c**, Tilted view (~15°) macroscopic optical images of three different 3D NIMs printed using a single stamp. **d**, Corresponding representative small-area SEM views of these three samples.

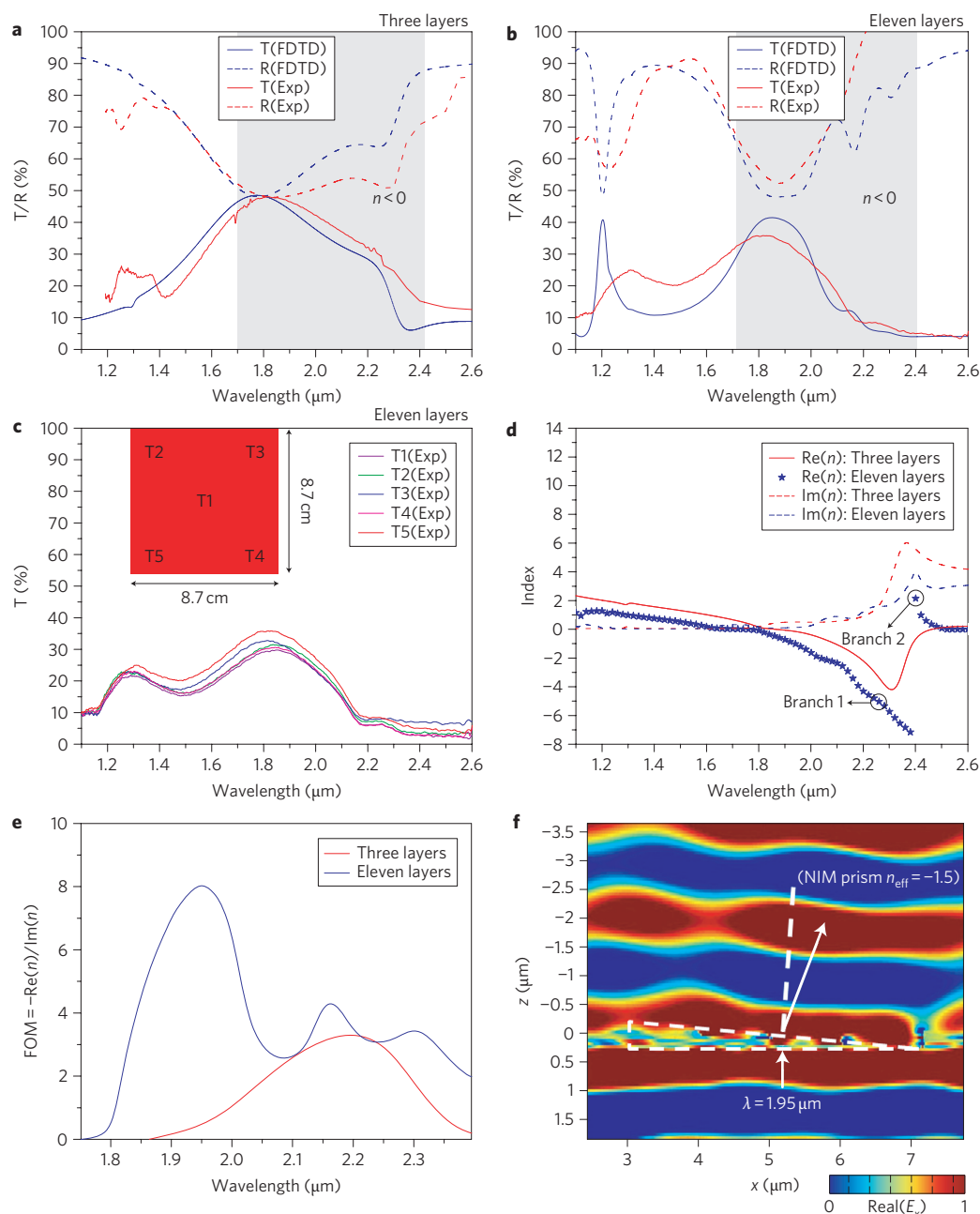


Figure 4 | Experimental measurements and simulation results for transmission/reflection and refractive indices of 3D NIMs. **a,b**, Experimental and FDTD results for transmission (T) and reflection (R) spectra of a three-layer NIM monolayer (**a**) and an eleven-layer 3D NIM (**b**). **c**, Transmission spectra collected from five different locations across the entire area of a 8.7 cm \times 8.7 cm, eleven-layer 3D NIM. **d**, Corresponding retrieved indices for three and eleven layers showing a negative index of refraction in the NIR band. **e**, FOM of three- and eleven-layer 3D NIM structures. **f**, The 4.48° NIM prism showing negative-phase propagation at $\lambda = 1.95 \mu\text{m}$. In all cases, $P = 850 \text{ nm}$, depth-averaged $W_x = 635 \text{ nm}$ and $W_y = 225 \text{ nm}$, Ag thickness = 30 nm, MgF_2 thickness = 50 nm, and background refractive index $n_s = 1.2$.

compatible with a range of flexible and rigid substrate materials. The stamps can be reused to produce many such NIMs structures in a manufacturing mode. The three frames of Fig. 3c show three copies produced using a single stamp, in a repetitive application of the process outlined in Fig. 1a; corresponding representative small-area SEM views of these three samples are shown in Fig. 3d. Visual inspection of the samples and high-resolution images collected from them indicate excellent spatial uniformity and low defect density. (The red and rainbow colours observed in these images are due to diffraction.)

The optical properties can be quantified by spatially resolved spectral measurements of transmission and reflection. Figure 4 shows experimentally measured and finite-difference time-domain

(FDTD) computed average transmission/reflection values for unpolarized light with 3D NIMs that have geometries reported above having three (Fig. 4a) and eleven (Fig. 4b) layers. Partial infiltration of openings in the mesh structure by the adhesive material (PDMS) used in the printing process (Fig. 2b) increases the background refractive index n_s . This effect moves the optical response to a higher wavelength range compared with the case with air as the background medium¹⁴. We used $n_s = 1.2$ in the FDTD simulation. If needed, this redshift can be counteracted by suitable choice of fishnet widths (W_x and W_y)¹⁴ or printing on less sticky substrates or using adhesiveless transfer techniques³¹. The FDTD simulations used averages of transmission/reflection separately computed with

planewave sources of light having transverse electric (TE) and transverse magnetic (TM) polarizations, to compare with the unpolarized light used in the spectrometer. Changes in optical responses associated with non-vertical sidewall growth can be compensated by appropriate modifications to the lateral dimensions of the structures on the stamps. We used stamps with dimensions $W_x \approx 565$ nm and $W_y \approx 170$ nm for the eleven-layer case, and $W_x \approx 600$ nm and $W_y \approx 200$ nm for the three-layer case, to achieve similar depth-averaged dimensions with an 8° sidewall ($W_x = 635$ nm and $W_y = 225$ nm). Both three- and eleven-layer samples show good agreement between experiment and simulation. The original theoretical work on these types of 3D NIMs suggests that a minimum of two unit cells (five layers) is required to achieve the necessary mutual inductance coupling between layers¹⁴. Samples with two different multilayer stacks (three and eleven layers) enable comparison of optical properties between a monolayer NIM (three layers) and a 3D NIM (11 layers). The results reveal the scaling of properties with numbers of layers, and also validate the correspondence between theory and experiment. The high spatial uniformity of the properties of even the largest 3D NIM that we fabricated are corroborated by transmission measurements collected at multiple locations (Fig. 4c). These data and simulation results can be used to retrieve the impedance (z) and refractive index (n) of the samples, as shown in Fig. 4d. The retrieval method used effective medium approaches, as described elsewhere^{32–34}. As confirmation of the correct identification of the branches of this inverse problem, we note that analysis of the two NIM thicknesses (that is, three and eleven layers) yields the same values for z and n (Fig. 4d). Figure 4d shows that the real part of the refractive index $\text{Re}(n)$ is negative between $1.75 \mu\text{m}$ and $2.4 \mu\text{m}$, with a minimum of approximately -4.2 and -7.8 for the three- and eleven-layer samples, respectively. The value is positive for wavelengths longer than $2.4 \mu\text{m}$, consistent with causality and passive medium requirements that $\text{Re}(z) > 0$ and $\text{Im}(n) > 0$ over the entire spectral range between $1.2 \mu\text{m}$ and $3 \mu\text{m}$ (Supplementary Fig. S6). The transmission/reflection measurements and retrieved parameters closely match theoretical predictions for structures of this type¹⁴. Figure 4d suggests that as the number of layers increases from three to eleven, the real part of the refractive index displays a large discontinuity at $2.4 \mu\text{m}$. As noted previously¹⁴, these two branches can be shown to result from different spatial modes¹⁴. The losses can be estimated through a FOM ($-\text{Re}(n)/\text{Im}(n)$) calculation, where FOM is inversely related to $\text{Im}(n)$ (that is, a measure of material loss). In other words, higher $\text{Im}(n)$ implies increased loss and reduced FOM. Figure 4e shows the results, which indicate that the three- and eleven-layer structures have maximum FOM values of ~ 3.5 (at $2.2 \mu\text{m}$) and ~ 8 (at $1.95 \mu\text{m}$), respectively (FOM is ~ 2 at the largest value of negative $\text{Re}(n) \approx -7.8$ for the eleven-layer NIM at a wavelength of $2.4 \mu\text{m}$). This reduction in loss with increasing numbers of layers is consistent with the prediction that cascading leads to strong magneto-inductive coupling between neighbouring functional layers through mutual inductances resulting in a broadband negative index of refraction with low loss^{14,17}. We verified the negative phase propagation by using FDTD to simulate the passage of plane waves through a 4.48° NIM prism. Figure 4f presents a single snapshot of the time evolution of the real part of the electric field component ($\text{Re}(E_x)$) as a function of space ($x-z$); a negatively tilted field phase front emerging from the NIM prism is apparent, as expected for this wavelength range. Such NIM prisms can be fabricated by FIB milling⁴ of a printed NIM, whereas angled deposition or ion-milling over/through shadowing structures represent other, more scalable, possibilities.

The results presented here suggest that, when implemented with automated tools, these simple printing techniques can be used for nanomanufacturing large-area 3D NIMs in a realistic manner.

Easy access to materials at such scales (more than seven orders of magnitude larger than previous reports) should accelerate the adoption of these and related NIMs technologies. The same basic approaches may also create new opportunities for NIMs designs that cannot be achieved in any other way. For example, folding or multilayer printing could yield NIMs with macroscopic thicknesses, embedded gain media, cavity defects or other structures. Combining these printing procedures with other large-area lithography techniques also seems promising. The results may allow NIMs designers to lift previous constraints associated with more conventional lithographic approaches.

Methods

Silicon stamp fabrication. The silicon was etched using a Bosch process (etch/passivation: cycle time, 5 s/5 s; RIE power, 20 W/0 W, $\text{SF}_6/\text{C}_4\text{F}_8$ flow rate, 35 s.c.c.m./110 s.c.c.m. for constant ICP power of 600 W; etch rate, $1 \mu\text{m}/80$ s) with SF_6 gas, to a depth between 1 and $2 \mu\text{m}$, through a mask formed by soft nanoimprint lithography. The moulds for this process consisted of elements of PDMS (Dow Corning, Sylgard) formed by casting and curing against a large-area pattern of photoresist defined on a silicon wafer by deep UV projection-mode photolithography. Detailed descriptions appear in the Supplementary Information.

Electron-beam deposition. Multilayer stacks were deposited using a Temescal (FC-1800) six-pocket electron-beam evaporation system. For optimal collimation, a small filament (~ 6 mm) was used. The sample was mounted almost vertically to the source, so that the evaporated flux front remained as normal as possible to the surface of the stamp. For deposition of SiO_2 , Ag and MgF_2 , average chamber pressures of $\sim 1.5 \times 10^{-6}$ and deposition rates of ~ 0.1 – 0.15 nm s^{-1} were found to yield the best film quality. The line edge roughness (LER) of the stamp and the top layer of the eleven-layer stack were ~ 10 nm and ~ 20 nm, respectively (the LER was estimated from analysis of high-resolution SEM images). As discussed in the main text, neither this LER nor the angled sidewall geometry had significant effects on the properties.

Printing the multilayer stack. The printing process involved careful introduction of dilute HF (5% in deionized water) onto the stamp to eliminate the sacrificial SiO_2 layer. A flat slab of PDMS or a PDMS-coated substrate was then contacted to the stamp and peeled off to complete the transfer. The 3D NIM stack on PDMS could, if desired, be printed onto another substrate (Supplementary Fig. S2). A key feature of the procedures is that they involve only low-temperature steps, with pristine, unaltered materials for the NIMs structures; they avoid chemical, thermal or other forms of degradation that can be introduced by lithographic processing, deep etching and other steps in alternative approaches. These aspects allow compatibility with low-cost substrates (such as plastics) and they may also contribute to the excellent optical properties of the resulting 3D NIMs, as highlighted above and described subsequently.

Optical measurements. Transmission/reflection spectra were collected using a $\times 10$ – $\times 10$, 0.1 numerical aperture objective on an optical microscope (Hyperion 2000) coupled to a Fourier-transform infrared spectrometer (Vertex 70) and outfitted with a spatial aperture with a diameter of 3.75 mm. Reflection spectra were normalized to a silver mirror with 96% reflectivity. Transmission spectra were normalized using a bare substrate.

FDTD simulation. Transmission and reflection spectra were calculated using experimental parameters for the printed 3D NIMs structures, with commercial FDTD software package (Lumerical, Lumerical Solutions Inc.). A Drude model was used for the dielectric parameters of silver in the FDTD simulation, with a plasma frequency of 9.0 eV and scattering frequency of 0.054 eV. The scattering frequency was increased by a factor of three compared with that of bulk silver to account for the additional surface scattering loss³⁵. The good agreement between experiment and FDTD results, which assume ideal geometries and zero LER, suggests that the observed losses are intrinsic to the materials and stack geometries used here. Slight variabilities in the dimensions of the structures, the properties of the constituent materials and the levels of control (such as uniformity and edge roughness) associated with the fabrication are the probable causes of the 10–15% overall discrepancy between experimental observation and FDTD simulation. We found that transmission through the 3D NIMs deviates strongly ($>30\%$) from FDTD predictions for structures with more than ~ 15 layers, limited by the non-vertical sidewall geometries discussed previously. The development of optimized physical vapour deposition techniques that can achieve more ideal sidewall shapes is a topic of current work.

Received 18 March 2011; accepted 27 April 2011;
published online 5 June 2011

References

- Veselago, V. G. The electrodynamics of substances with simultaneously negative values of ϵ and μ . *Sov. Phys. Usp.* **10**, 509–514 (1968).
- Pendry, J. B. Negative refraction makes a perfect lens. *Phys. Rev. Lett.* **85**, 3966–3969 (2000).
- Shelby, R. A., Smith, D. R. & Schultz, S. Experimental verification of a negative index of refraction. *Science* **292**, 77–79 (2001).
- Valentine, J. *et al.* Three-dimensional optical metamaterial with a negative refractive index. *Nature* **455**, 376–380 (2008).
- Liu, N. *et al.* Three-dimensional photonic metamaterials at optical frequencies. *Nature Mater.* **7**, 31–37 (2007).
- Enoch, S., Tayeb, G., Sabouroux, P., Guérin, N. & Vincent, P. A Metamaterial for directive emission. *Phys. Rev. Lett.* **89**, 213902 (2002).
- Silveirinha, M. & Engheta, N. Tunneling of electromagnetic energy through subwavelength channels and bends using ϵ -near-zero materials. *Phys. Rev. Lett.* **97**, 157403 (2006).
- Edwards, B., Alu, A., Young, M. E., Silveirinha, M. & Engheta, N. Experimental verification of ϵ -near-zero metamaterial coupling and energy squeezing using a microwave waveguide. *Phys. Rev. Lett.* **100**, 033903 (2008).
- Paul, O., Imhof, C., Reinhard, B., Zengerle, R. & Beigang, R. Negative index bulk metamaterial at terahertz frequencies. *Opt. Express* **16**, 6736–6744 (2008).
- Awad, M., Nagel, M. & Kurz, H. Negative-index metamaterial with polymer-embedded wire-pair structures at terahertz frequencies. *Opt. Lett.* **33**, 2683–2685 (2008).
- Dolling, G., Enkrich, C. & Wegener, M. Low-loss negative-index metamaterial at telecommunication wavelengths. *Opt. Lett.* **31**, 1800–1802 (2006).
- Alu, A. & Engheta, N. Three-dimensional nanotransmission lines at optical frequencies: a recipe for broad band negative-refraction optical metamaterials. *Phys. Rev. B* **75**, 024304 (2007).
- Dolling, G., Wegener, M. & Linden, S. Realization of a three-functional-layer negative-index photonic metamaterial. *Opt. Lett.* **32**, 551–553 (2007).
- Zhang, S. *et al.* Optical negative-index bulk metamaterials consisting of 2D perforated metal–dielectric stacks. *Opt. Express* **14**, 6778–6787 (2006).
- Dutta, N., Mirza, I. O., Shi, S. & Prather, D. W. Fabrication of large area fishnet optical metamaterial structures operational at near-IR wavelengths. *Materials* **3**, 5283–5292 (2010).
- Zhang, S. *et al.* Near-infrared double negative metamaterials. *Opt. Express* **13**, 4922–4930 (2005).
- Li, T. *et al.* Coupling effect of magnetic polariton in perforated metal/dielectric layered metamaterials and its influence on negative refraction transmission. *Opt. Express* **14**, 11115–11163 (2006).
- Eleftheriades, G. V. Analysis of bandwidth and loss in negative-refractive-index transmission-line (NRI-TL) media using coupled resonators. *IEEE Microw. Wireless Components Lett.* **17**, 412–414 (2007).
- Chou, S. Y., Krauss, P. R. & Renstrom, P. J. Nanoimprint lithography. *J. Vac. Sci. Technol. B* **14**, 4129–4133 (1996).
- Costner, E. A., Lin, M. W., Jen, W. L. & Willson, C. G. Nanoimprint lithography materials development for semiconductor device fabrication. *Annu. Rev. Mater. Res.* **39**, 155–180 (2009).
- Xia, Y., Rogers, J. A., Paul, K. E. & Whitesides, G. M. Unconventional methods for fabricating and patterning nanostructures. *Chem. Rev.* **99**, 1823–1848 (1999).
- Gates, B. D., Xu, Q., Love, J. C., Wolfe, D. B. & Whitesides, G. M. Unconventional nanofabrication. *Annu. Rev. Mater. Res.* **34**, 339–372 (2004).
- Lee, M. H., Huntington, M. D., Zhou, W., Yang, J. & Odom, T. W. Programmable soft lithography: solvent-assisted nanoscale embossing. *Nano Lett.* **11**, 311–315 (2011).
- Rolland, J. P., Hagberg, E. C., Carter, K. R. & DeSimone, J. M. High resolution soft lithography: enabling materials for nano-technologies. *Angew. Chem. Int. Ed.* **43**, 5796–5799 (2004).
- LaFratta, C. N., Li, L. & Fourkas, J. T. Soft-lithographic replication of 3D microstructures with closed loops. *Proc. Natl Acad. Sci. USA* **103**, 8589–8594 (2006).
- Hill, D. N., Lee, J. D., Cochran, J. K. & Chapman, A. T. Vapour deposited cone formation during fabrication of low voltage field emitter array cathodes. *J. Mater. Sci.* **31**, 1789–1796 (1996).
- Lee, H., Park, Y., Kim, J., Choi, J. & Kim, J. Investigation of the formation mechanism of Spindt-type cathode by simulation and experiments. *J. Vac. Sci. Technol. B* **17**, 547–551 (1999).
- Melik, R., Unal, E., Perkgoz, N. K., Puttlitz, C. & Demir, H. V. Flexible metamaterials for wireless strain sensing. *Appl. Phys. Lett.* **95**, 181105 (2009).
- Falco, A. D., Ploschner, M. & Krauss, T. F. Flexible metamaterials at visible wavelengths. *New J. Phys.* **12**, 113006 (2010).
- Peralta, X. G. *et al.* Large-area metamaterials on thin membranes for multilayer and curved applications at terahertz and higher frequencies. *Appl. Phys. Lett.* **94**, 161113 (2009).
- Meitl, M. A. *et al.* Transfer printing by kinetic control of adhesion to an elastomeric stamp. *Nature Mater.* **5**, 33–38 (2006).
- Smith, D. R., Schultz, S., Markos, P. & Soukoulis, C. M. Determination of effective permittivity and permeability of metamaterials from reflection and transmission coefficients. *Phys. Rev. B* **65**, 195104 (2002).
- Chen, X., Grzegorzczak, T. M., Wu, B. L., Pacheco, J. Jr & Kong, J. A. Robust method to retrieve the constitutive effective parameters of metamaterials. *Phys. Rev. E* **70**, 016608 (2004).
- Smith, D. R., Vier, D. C., Koschny, T. & Soukoulis, C. M. Electromagnetic parameter retrieval from inhomogeneous metamaterials. *Phys. Rev. E* **71**, 036617 (2005).
- Johnson, P. B. & Christy, R. W. Optical constants of the noble metals. *Phys. Rev. B* **6**, 4370–4379 (1972).

Acknowledgements

The work at University of Illinois was supported by a grant from the Office of Naval Research. The authors also gratefully acknowledge the contribution of Sandia National Laboratory, which is a multi-programme laboratory operated by Sandia Corporation, a Lockheed Martin Company, for the US Department of Energy (contract no. DE-AC04-94AL85000), in fabricating the large-area master mask using deep UV lithography.

Author contributions

D.C. conceived the idea and designed experiments. J.A.R. provided technical guidance. D.C., K.S. and T.C. performed the experiments. D.C. measured, analysed and simulated the data. G.R.B., S.G., A.M., A.C., A.B. and P.B. contributed materials and analysis tools. D.C. and J.A.R. co-wrote the paper.

Additional information

The authors declare no competing financial interests. Supplementary information accompanies this paper at www.nature.com/naturenanotechnology. Reprints and permission information is available online at <http://www.nature.com/reprints/>. Correspondence and requests for materials should be addressed to J.A.R.

Large-area, flexible 3D optical negative index metamaterial formed by nanotransfer printing

Debashis Chanda¹, Kazuki Shigeta¹, Sidhartha Gupta¹, Tyler Cain¹, Andrew Carlson¹, Agustin Mihi¹, Alfred Baca³, Gregory R. Bogart⁴, Paul Braun¹, John A. Rogers^{1,2*}

Supplementary Information:

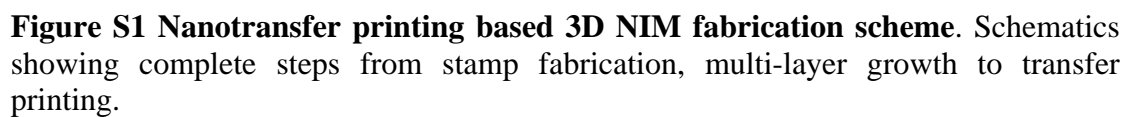
Methods

Silicon stamp fabrication. Diluted (8% wt) photoresist (SU-8 monomer; MicroChem) in cyclopentanol was spin cast (500 rpm for 5 s followed by 2000 rpm for 30 s) on a silicon wafer (Montco Silicon) coated with silicon nitride (~200 nm using PECVD). Soft imprint lithography with molds of poly(dimethylsiloxane) formed patterns in the SU-8. The PDMS molds resulted from the casting and curing techniques of soft lithography with masters consisting of silicon wafers with patterns of photoresist formed by deep ultraviolet projection mode photolithography. The regions of the silicon nitride not protected by the SU-8 were removed by reactive ion etching (RIE) (Plasma-Therm) using CF₄. Next, the exposed silicon was etched using inductively coupled plasma RIE (ICP-RIE, Plasma-Therm) in a Bosch process (etch/passivation: cycle time = 5 sec/5 sec, RIE power = 20W/0W, SF₆/C₄F₈ flow rate = 35 sccm/20 sccm for constant ICP power = 600 W. Etch rate 1 μm/80sec) with SF₆ gas, to a depth between 1 and 2 μm. The stamp fabrication was completed by removing the SU-8 and silicon nitride by dipping into a piranha solution (H₂SO₄:H₂O₂ = 3:1) for 15 min and then into diluted HF (25%) for 5 sec followed by sonication in acetone (5 min). The detailed steps appear in Fig. S1.

Printing the multilayer stack. The printing process involved careful introduction of dilute HF (5% in DI water) onto the stamp through a stack (4-5) of porous paper cloths (TX 1109

TechniCloth II, ITWTexwipe), as shown in Fig. S2. After ~30 min, the cloths were removed one after one and a flat slab of PDMS (Dow Corning, Sylgard) was contacted to the NIM stack and then peeled off to complete the transfer. The 3D NIM stack on PDMS can, if desired, be printed onto another substrate, as shown in Fig. S2. The stamp was first cleaned by rinsing with 5% HF (diluted with DI water), and then DI water. The procedure was then repeated with rinsing in acetone and then DI water, followed by drying with N₂.

Finite difference time domain modeling. The FDTD simulations used averages of transmission/reflection separately computed with plane wave sources of TE and TM polarizations, to compare with the unpolarized light used in the spectrometer. These simulations used precise geometries extracted from images such as the one in Fig. 2b, but without any LER. These modeling results are consistent with those that use vertical sidewalls but depth-averaged dimensions. See Fig. S5.



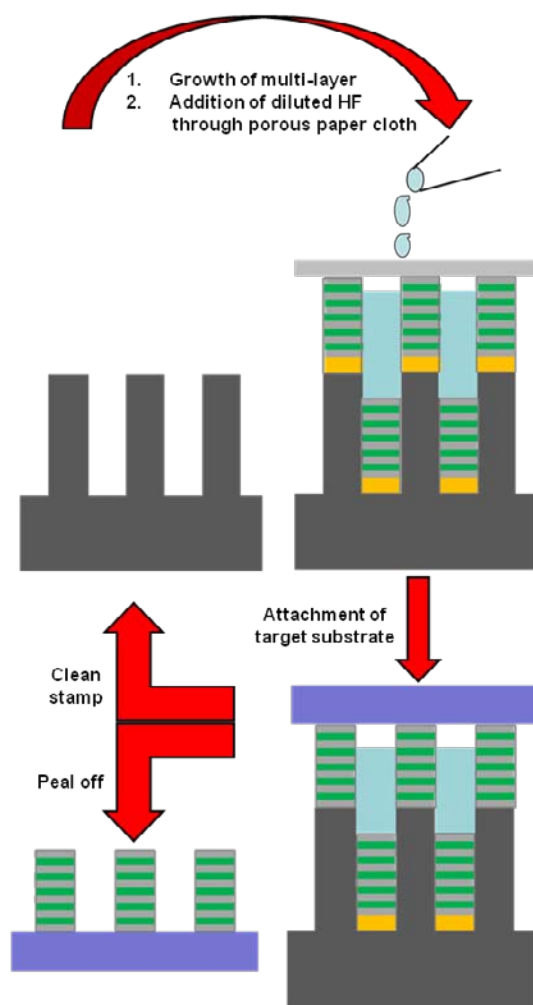


Figure S2 Transfer of multi-layer stack to a target substrate. Steps showing release of multi-layer stack from the stamp to the target substrate.

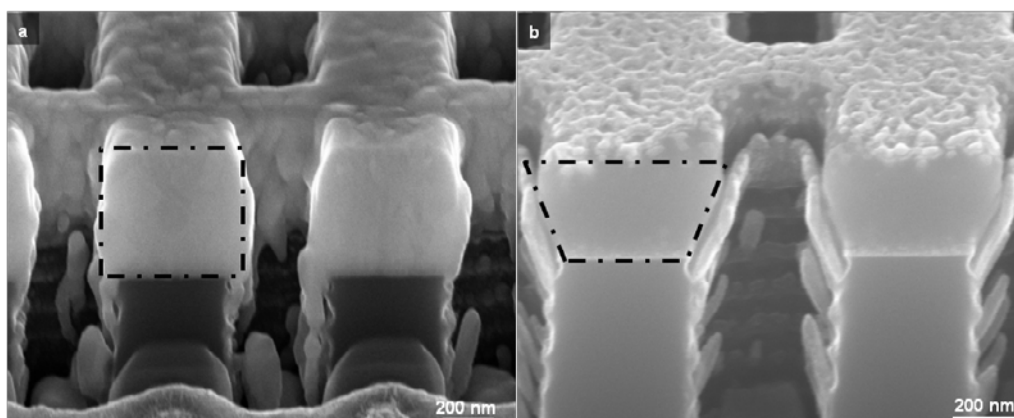


Figure S3 Estimation of angular growth. The 52° tilted SEM view of FIB milled single ~400 nm layer growth of (a) Ag and (b) MgF₂ on the silicon stamp.

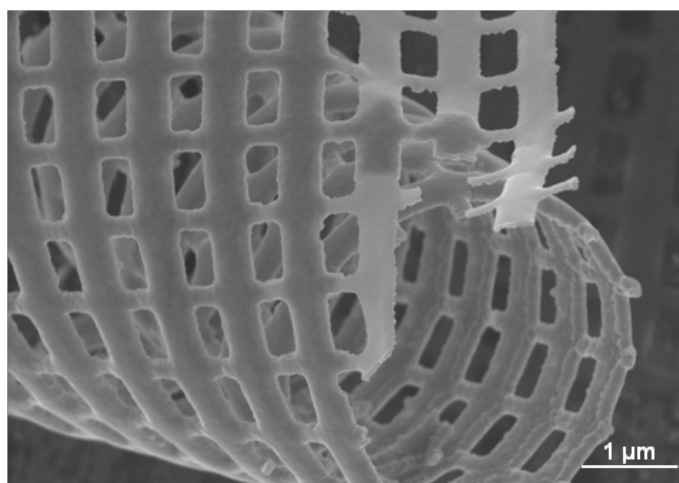


Figure S4 Free standing 3D NIM. The picked up free standing 3D NIM where a mild adhesive surface (scotch tape) was used to pick up the free standing 3D stack.

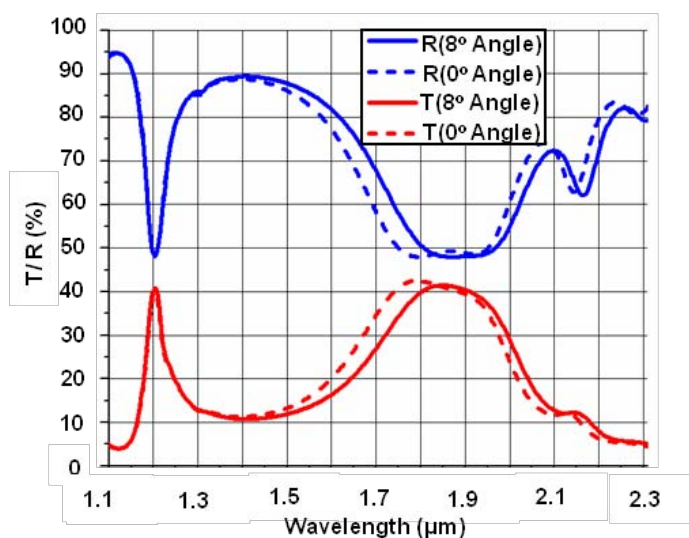


Figure S5 FDTD computed average T/R with and without small angular (8°) growth. FDTD predicted transmission and reflection spectra of an 11-layer 3D NIM with and without small angular (8°) growth structures with $P = 850$ nm, and depth-averaged $W_x = 635$ nm and $W_y = 225$ nm. Ag thickness = 30 nm, MgF_2 thickness = 50 nm and background refractive index $n_s = 1.2$.

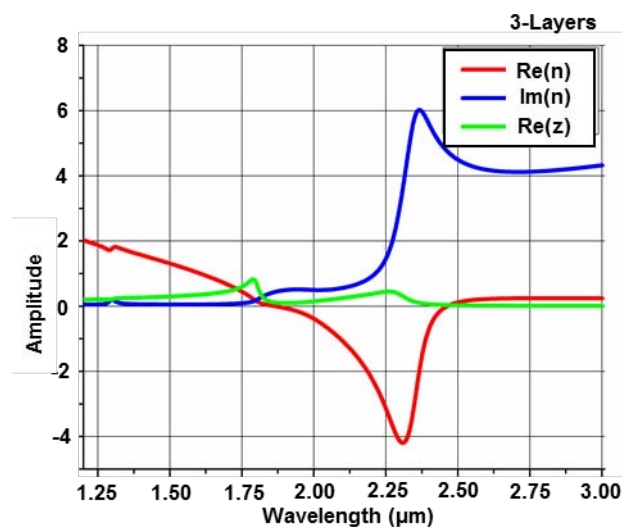


Figure S6 Retrieved index and impedance of 3-layer Fishnet. Retrieve indices showing the real ($\text{Re}(n)$) and imaginary ($\text{Im}(n)$) parts of the refractive index and the real part of the impedance ($\text{Re}(z)$).